Interaction between counterpropagating Rossby waves and capillary waves in planar shear flows

L. Biancofiore, F. Gallaire, and E. Heifetz

Citation: Physics of Fluids **27**, 044104 (2015); doi: 10.1063/1.4916285
View online: http://dx.doi.org/10.1063/1.4916285
View Table of Contents: http://scitation.aip.org/content/aip/journal/pof2/27/4?ver=pdfcov
Published by the AIP Publishing

PHYSICS OF FLUIDS **27**, 044104 (2015)

Interaction between counterpropagating Rossby waves and capillary waves in planar shear flows

L. Biancofiore,[1] F. Gallaire,[2] and E. Heifetz[3]
[1]*Department of Mechanical Engineering, Imperial College London, Exhibition Road, South Kensington, London SW7 2AZ, United Kingdom*
[2]*EPFL / LFMI, Route Cantonale, Lausanne, Switzerland*
[3]*Department of Geophysics and Planetary Sciences, Tel-Aviv University, Ramat-Aviv, Tel-Aviv 69978, Israel*

(Received 23 October 2014; accepted 16 March 2015; published online 10 April 2015)

A counterintuitive destabilizing effect of the surface tension in planar wakes has been observed by Tammisola *et al*. ["Effect of surface tension on global modes of confined wake flows," Phys. Fluids **23**, 014108 (2011)] and Biancofiore *et al*. ["Direct numerical simulations of two-phase immiscible wakes," Fluid Dyn. Res. **46**, 041409 (2014)] by means of linear global analyses and direct numerical simulations, respectively. In the present study, we approximate the velocity profile of a wake flow through a piecewise broken-line profile and explain the presence of temporal unstable modes using an interfacial wave interaction perspective. With this perspective, we associate to each vorticity discontinuity an individual counterpropagating Rossby wave (RW), while the introduction of a finite amount of surface tension at the interface creates two capillary waves (CWs) which propagate with respect to the interface velocity with the same relative velocity but in opposite directions. The addition of the surface tension generates a new unstable mode, which is a Rossby-capillary mode, since it is due to the interaction between one RW and one CW. Furthermore, we capture the spatio-temporal evolution of the interacting four-waves system by means of an impulse response analysis. The spreading of the wavepacket, and consequently the absolute nature of the instability, is enhanced by a moderate surface tension, especially if the interface is located close to the faster edge of the broken-line wake profile. This can be explained by the influence of the surface tension on the group velocities of the waves, taken in isolation. © *2015 AIP Publishing LLC.* [http://dx.doi.org/10.1063/1.4916285]

I. INTRODUCTION

Surface tension acts as a restoring force which minimizes the contact area between the fluids. Due to these restoring properties, it is therefore viewed as a stabilizing agent in plane shear flows. Recently, a counterintuitive destabilisation due to the surface tension was noticed by Tammisola *et al*.[1] in planar wakes by means of global linear analysis. The same authors have extended their analysis to two-phase jets[2] showing the same destabilisation effect. Furthermore, they have found that both sinuous and varicose perturbations are destabilised by capillary forces. Biancofiore *et al*.[3] confirmed the destabilising influence of the surface tension in planar wake by means of direct numerical simulations (DNSs), using a level-set formulation for the interface-capturing. However, only the sinuous mode was found to be destabilised. This surprising destabilisation effect by surface tension is relevant to technological applications, where two or more co-flowing parallel flow sheets meet and interact (as in paper making processes[4]).

Unrelatedly, the concept of counterpropagating Rossby waves (RWs) has been developed originally by Bretherton[5] to explain the baroclinic instability mechanism for cyclone development in the atmosphere. He showed that the instability in flows featuring two distinct potential vorticity gradients can be interpreted in terms of the interaction between two distinct Rossby edge waves. Such waves were coined counterpropagating by Hoskins *et al*.[6] since their propagation direction is opposite to their local mean flow. Although each wave by itself is neutral, the mutual interaction yields an instability

through a phase-locking mechanism. Depending on their phase difference, each RW modifies the propagation rate of the other and also promotes its growth. Growing normal modes are obtained in a suitable phase difference when the interaction makes the RWs to propagate with the same phase speed and to have the same growth rate.

More recently, the interaction of these RWs has been implemented by Heifetz *et al.*[7] to describe the instability in an unconfined inviscid mixing layer of a finite shear layer thickness. Biancofiore and Gallaire[8] further exported the counterpropagating RW concept from the geophysics community to the fluid mechanics one, as they employed this paradigm to explain the instability in confined plane wakes in terms of RW interaction. Harnik *et al.*[9] generalized further the RW interaction in a distance mechanism to interfacial vorticity waves whose propagation mechanism can be different from the advection of mean vorticity. They showed how the buoyancy restoring force, in stably stratified shear flow, generates interfacial vorticity waves and how the interaction between such two remote counter-propagating vorticity buoyancy waves yields instability. This concept has been used by Rabinovich *et al.*[10] to interpret the counter-intuitive results of how stable stratification may destabilize a shear flow.[11] Moreover, in setups which include both mean vorticity and density gradients (such as the Holmboe[12] one), the instability has been interpreted in terms of action at a distance between Rossby and buoyancy-driven interfacial vorticity waves.[13]

In this work, we suggest that in small scales the restoring force of surface tension between two immiscible fluids can generate as well interfacial vorticity waves. Similar to the buoyancy waves, the interaction at distance between such interfacial capillary waves and/or between interfacial Rossby ones may lead to instability. In order to illustrate the instability mechanism, we revisit the piecewise linear profile of a plane wake discussed in Biancofiore and Gallaire.[8] In the present context, the flow is however composed of three immiscible fluids (Fig. 1).

The paper is organized as follows. In Sec. II, we present the setup of the model and the formulation of the governing linearised equations in terms of vorticity and displacement. Then in Sec. III, we analyse the behaviour of the interfacial Rossby and capillary waves in isolation, and the modal instability results from the phase-locking interaction in a distance between those interfacial waves. This method of solution is compared with the standard one, based on matching conditions, in the Appendix. In Secs. IV and V, we analyse the normal modes in terms of the interacting vorticity waves by means of a temporal and a spatio-temporal analyses. Finally, conclusion and perspectives are drawn in Sec. VI.

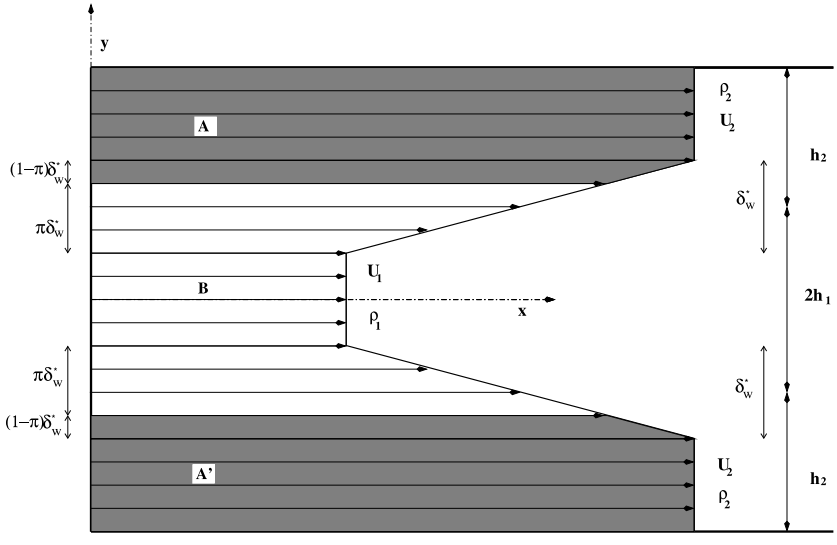

FIG. 1. The model consists of three flows sandwiched between two flat plates including the surface tension acting at the interfaces.

II. MODEL SETUP AND GOVERNING EQUATIONS

A. The basic state

The model flow consists of one inner fluid (B) sandwiched between two layers of the same immiscible fluid (A and A') confined between two flat plates, as illustrated in Figure 1. The inner flow (B) has width $2[h_1 + \delta_w^*(\alpha - \frac{1}{2})]$, where α is a parameter $0 \le \alpha \le 1$, while the outer flows (A and A') have the same width $h_2 + \delta_w^*(\frac{1}{2} - \alpha)$. The two fluids are assumed incompressible and inviscid. Hence, both the no-slip boundary condition on the walls and the tangential boundary conditions on the interface are relaxed. A restoring force due to surface tension σ is assumed at the interfaces between the immiscible fluids, whose positions are controlled by the parameter α, $y_\alpha = \pm[h_1 + \delta_w^*(\alpha - \frac{1}{2})]$.

The dimensional velocity profile of the model flow is

$$U(y) = \begin{cases} U_2 & \text{for} \quad h_1 + \dfrac{\delta_w^*}{2} \le |y| \le h_1 + h_2 \\ U_2 - \dfrac{(U_1 - U_2)}{\delta_w^*}[|y| - (h_1 + \dfrac{\delta_w^*}{2})] & \text{for} \quad h_1 - \dfrac{\delta_w^*}{2} < |y| < h_1 + \dfrac{\delta_w^*}{2} \\ U_1 & \text{for} \quad |y| \le h_1 - \dfrac{\delta_w^*}{2} \end{cases}. \tag{1}$$

Using h_1 and $U_m = (U_1 + U_2)/2$ as reference length and velocity scales, respectively, we construct the following non-dimensional parameters. The confinement parameter is $h = h_2/h_1$, the shear layer thickness is $\delta_w = \delta_w^*/h_1$, and $\Lambda = (U_1 - U_2)/(U_1 + U_2)$ is the velocity ratio. In general, wake flows have negative velocity ratios while jet flows have positive ones. When $0 < |\Lambda| < 1$, a co-flow configuration is modeled, and while $|\Lambda| > 1$, it is a counter-flow setup. Using this set of scales and omitting the asterisks hereafter, the non-dimensional velocity profile becomes

$$U(y) = \begin{cases} 1 - \Lambda & \text{for} \quad 1 + \dfrac{\delta_w}{2} \le |y| \le 1 + h \\ 1 - \Lambda + m[|y| - (1 + \dfrac{\delta_w}{2})] & \text{for} \quad 1 - \dfrac{\delta_w}{2} < |y| < 1 + \dfrac{\delta_w}{2} \\ 1 + \Lambda & \text{for} \quad |y| \le 1 - \dfrac{\delta_w}{2} \end{cases}, \tag{2}$$

where $m = -2\Lambda/\delta_w$. The non-dimensional basic piecewise vorticity profile $Q = -dU/dy$ reads

$$Q(y) = \begin{cases} 0 & \text{for} \quad 1 + \dfrac{\delta_w}{2} < |y| < 1 + h \\ -m & \text{for} \quad 1 - \dfrac{\delta_w}{2} < y < 1 + \dfrac{\delta_w}{2} \\ 0 & \text{for} \quad |y| < 1 - \dfrac{\delta_w}{2} \\ m & \text{for} \quad -(1 + \dfrac{\delta_w}{2}) < y < -(1 + \dfrac{\delta_w}{2}) \\ 0 & \text{for} \quad -(1 + h) < y < -(1 + \dfrac{\delta_w}{2}) \end{cases}. \tag{3}$$

B. Vorticity-displacement formulation

We begin with the non-dimensional momentum and continuity equation linearized with respect to (2),

$$\frac{Du}{Dt} = -vU_y - \frac{\partial p}{\partial x}, \tag{4a}$$

$$\frac{Dv}{Dt} = \Sigma C - \frac{\partial p}{\partial y}, \tag{4b}$$

$$C = \kappa\delta(y - y_\alpha), \tag{4c}$$

$$\frac{\partial u}{\partial y} + \frac{\partial v}{\partial x} = 0, \tag{4d}$$

where $(D/Dt) \equiv (\partial/\partial t) + U(\partial/\partial x)$, $\mathbf{u} = (u, v)$ is the perturbation velocity vector, and p is the perturbation pressure. $\Sigma = \sigma/(h_1 \rho_m U_m^2)$ is the non-dimensional surface tension parameter, where ρ_m is the reference constant density. C is the capillary force, where $\kappa = \partial^2\zeta/\partial x^2$ is the approximated interface curvature, where ζ is the perturbation cross-stream displacement. δ symbolizes the Dirac delta function.

Taking the curl of Eqs. (4a) and (4b), we obtain

$$\frac{Dq}{Dt} = -vQ_y + \Sigma \frac{\partial \kappa}{\partial x}\delta(y - y_\alpha), \tag{5a}$$

$$\frac{D\zeta}{Dt} = v, \tag{5b}$$

where the perturbation vorticity $q = (\partial v/\partial x) - (\partial u/\partial y)$, and the mean cross-stream vorticity gradient is $Q_y = -U_{yy}$. For a single Fourier component with wavenumber k of the form e^{ikx}, the surface tension component at the RHS of (5a) becomes $-(k^2\Sigma)\frac{\partial \zeta}{\partial x}\delta(y - y_\alpha)$ and therefore, plays a similar role to the stably stratified buoyancy restoring force at the interface between two fluids with different densities (cf. Eqs. (2) and (13b) of Harnik *et al.*[9]). The mechanism by which interfacial restoring forces generate vorticity waves is shown in Figure 2 of Harnik *et al.*[9] in the case of gravity waves and can be generalized to capillary waves. The main difference between the two restoring forces is that the surface tension coefficient is proportional to k^2 and hence, efficient at small scales, whereas the buoyancy coefficient affects all wavenumbers equivalently.

Since $q = (\partial v/\partial x) - (\partial u/\partial y) = -k^2\psi + (\partial^2\psi/\partial y^2)$, where ψ is the perturbation streamfunction, equation set (5) can be expressed solely in terms of vorticity-displacement dynamics by introducing the Green's function $G(y, y', k)$, satisfying $-k^2 G + (\partial^2 G/\partial y^2) = -\delta(y - y')$. Then

$$v(y) = \partial\psi/\partial x = -ik \int_{y'} q(y')G(y, y', k)dy' \tag{6}$$

and

$$\frac{Dq}{Dt} = ikQ_y \int_{y'} q(y')G(y, y', k)dy' - ik^3\Sigma\zeta\delta(y - y_\alpha), \tag{7a}$$

$$\frac{D\zeta}{Dt} = -ik \int_{y'} q(y')G(y, y', k)dy'. \tag{7b}$$

The Green's function $G(y, y', k)$ depends on the boundary conditions. Since jets and wakes are symmetric with respect to the x-axis, two different perturbations can be distinguished: anti-symmetric varicose perturbations and symmetric sinuous ones. Since any perturbation can be composed of a linear combination of varicose and sinuous perturbations, we can study only one half of the domain illustrated in Figure 1. By imposing the Dirichlet condition $v(y = 0, 1 + h) = ik\ \psi = 0$, the varicose mode is obtained, while the sinuous mode is satisfied by imposing the Neumann condition $u(y = 0) = -\partial_y\ \psi = 0$ and the Dirichlet one at the wall $y = 1 + h$. The appropriate varicose and sinuous Green's functions are given, respectively, by

$$G_{vc}(y, y', k) = \frac{1}{k\sinh[k(1 + h)]} \begin{cases} \sinh(k\,y')\sinh[k(1 + h - y)] & \text{for} \quad y' \le y \le 1 + h \\ \sinh[k(1 + h - y')]\sinh(k\,y) & \text{for} \quad 0 \le y \le y' \end{cases}, \tag{8}$$

$$G_{si}(y, y', k) = \frac{1}{k\cosh[k(1 + h)]} \begin{cases} \cosh(k\,y')\sinh[k(1 + h - y)] & \text{for} \quad y' \le y \le 1 + h \\ \sinh[k(1 + h - y')]\cosh(k\,y) & \text{for} \quad 0 \le y \le y' \end{cases}. \tag{9}$$

In this paper, we are interested in demonstrating the instability mechanism between capillary and Rossby waves. Hence, we choose to focus hereafter only on the sinuous mode in order to compare the effect of surface tension with the study of Biancofiore and Gallaire[8] who examined the sinuous mode dynamics solely in terms of Rossby wave interaction.

III. INTERFACIAL WAVE INTERACTION PERSPECTIVE TO MODAL INSTABILITY

The dynamics of the phase-locking action at a distance between the two counterpropagating RW interfacial waves at $y = 1 \pm \frac{\delta_w}{2}$ is analyzed in detail in Biancofiore and Gallaire,[8] and the reader is kindly referred to this paper. In order to analyse the interaction of the two RWs with the capillary interfacial waves at $y_\alpha = \pm[1 + \delta_w(\alpha - \frac{1}{2})]$, we characterise first the dynamics of these capillary waves in isolation.

A. Interfacial capillary waves

In the absence of a mean vorticity gradient Q_y, Eq. (7a) implies that

$$q = q_\alpha(k,t)\delta[y - y_\alpha], \tag{10}$$

and therefore at y_α, Eq. (7) becomes

$$\frac{Dq_\alpha}{Dt} = -ik^3\Sigma\zeta, \tag{11a}$$

$$\frac{D\zeta}{Dt} = -ik\int_{y'} q_\alpha G_{\alpha,\alpha}dy', \tag{11b}$$

where $G_{\alpha,\alpha} = G(y_\alpha, y_\alpha) = \frac{\cosh[k(1+\delta_w(\alpha-\frac{1}{2}))]\cdot\sinh[k(h-\delta_w(\alpha-\frac{1}{2}))]}{k\cosh[k(1+h)]}$. Equation (11) can be rewritten in a matrix form,

$$\dot{\boldsymbol{\xi}} = \mathbf{M}_{CW}\boldsymbol{\xi}, \quad \text{where} \quad \boldsymbol{\xi} = \begin{bmatrix} q_\alpha \\ \zeta_\alpha \end{bmatrix} \quad \text{and} \quad \mathbf{M}_{CW} = -ik\begin{bmatrix} U_\alpha & k^2\Sigma \\ G_{\alpha\alpha} & U_\alpha \end{bmatrix}. \tag{12}$$

The eigenvalues of the matrix $\boldsymbol{M}_{CW}$ are $\lambda^\pm = -ikc^\pm = -ik[U_\alpha \pm k\sqrt{\Sigma G_{\alpha\alpha}}]$, where $c^\pm$ are the eastward and westward normal mode phase speeds. In the reference frame of the interface velocity $U_\alpha = U(y_\alpha)$, one of the capillary waves propagates downstream and is referred to as prograde +, while the other propagates upstream and is referred to as retrograde −. Since $G_{\alpha\alpha}$ scales like $2/k$ for $k > 1$, the intrinsic capillary wave velocity, which, respectively, adds to and reduces from the interface velocity, scales like $k^{1/2}$. This is best seen in Figure 2(b) where the intrinsic velocity of the two capillary waves is reported for $h = 1$, $\Lambda = -1$, $\delta_w = 0.5$, and $\alpha = 0.5$ and different values of $\Sigma = (0.05, 0.2, 0.5)$.

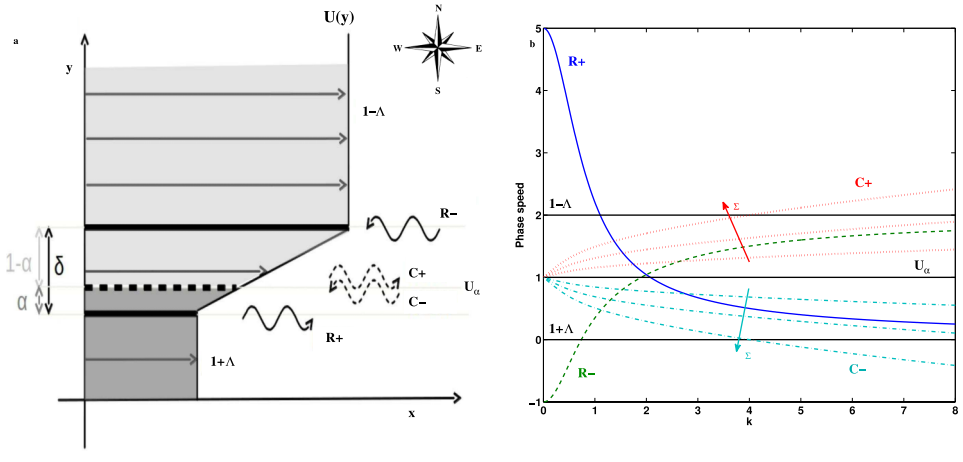

FIG. 2. (a) Sketch of the waves interacting in the piecewise broken line model including surface tension. We call $R-$ and $R+$ ($C-$ and $C+$) the Rossby wave (capillary wave) propagating westward and eastward, respectively. (b) Phase speeds of the wave in isolation for $h = 1$, $\Lambda = -1$, $\delta_w = 0.5$, and $\alpha = 0.5$. We have traced the curves for three different values of the surface tension $\Sigma = (0.05, 0.2, 0.5)$. The continuous line depicts $R+$, the dashed line depicts $R-$, the dotted one depicts $C+$, and the dashed-and-dotted line depicts $C-$.

These two waves correspond, respectively, to the eigenvectors

$$\boldsymbol{\xi}^{\pm} = \begin{bmatrix} 1 \\ \pm\sqrt{\dfrac{G_{\alpha\alpha}}{\Sigma k^2}} \end{bmatrix}. \tag{13}$$

An arbitrary $\boldsymbol{\xi}$ configuration can be uniquely divided into the two normal modes as follows:

$$\boldsymbol{\xi} = q_\alpha^+ \boldsymbol{\xi}^+ + q_\alpha^- \boldsymbol{\xi}^- \tag{14}$$

or equivalently in the matrix form, denoting by $\mathbf{q} = [q_\alpha^+; q_\alpha^-]$, the vector of coefficients in the basis of the eigenmodes

$$\boldsymbol{\xi} = \boldsymbol{T}\mathbf{q} = \begin{bmatrix} 1 & 1 \\ \sqrt{\dfrac{G_{\alpha\alpha}}{\Sigma k^2}} & -\sqrt{\dfrac{G_{\alpha\alpha}}{\Sigma k^2}} \end{bmatrix} \mathbf{q}. \tag{15}$$

The similarity transformation,

$$\dot{\mathbf{q}} = (\boldsymbol{T}^{-1}\boldsymbol{M}_{CW}\boldsymbol{T})\mathbf{q} = \bar{\boldsymbol{M}}_{CW}\mathbf{q}, \tag{16}$$

allows us to present the capillary waves dynamics solely in terms of the vorticity contributions of the respective eigenmodes $q_\alpha^{\pm}$, where

$$\bar{\boldsymbol{M}}_{CW} = -ik \begin{bmatrix} c^+ & 0 \\ 0 & c^- \end{bmatrix} \tag{17}$$

is the diagonal matrix consisting the eigenvalues of $\boldsymbol{M}_{CW}$.

B. Governing equations for the Rossby-capillary wave interaction

The mean vorticity gradient at the half domain of (3) is

$$Q_y = \pm m\delta[y - (1 \pm \frac{\delta_w}{2})]. \tag{18}$$

Hence, now the vorticity waves are localised in three levels at the upper part of the domain (cf. Fig. 2 for illustration): the interface between the immiscible fluids and the two jumps in the mean vorticity is

$$q = \left(q_1(k,t)\delta\big[y - 1 + \frac{\delta_w}{2}\big] + q_2(k,t)\delta\big[y - 1 - \frac{\delta_w}{2}\big] + q_\alpha(k,t)\delta[y - y_\alpha] \right), \tag{19}$$

where levels 1 and 2 correspond hereafter to $y_{1,2} = 1 \mp \frac{\delta_w}{2}$. Substitute Eqs. (18), (19), and (9) in Eq. (7) yields

$$\frac{\partial q_1}{\partial t} = -ik(1+\Lambda)q_1 + ikm(G_{11}q_1 + G_{12}q_2 + G_{1\alpha}q_\alpha), \tag{20a}$$

$$\frac{\partial q_2}{\partial t} = -ik(1-\Lambda)q_2 - ikm(G_{12}q_1 + G_{22}q_2 + G_{2\alpha}q_\alpha), \tag{20b}$$

$$\frac{\partial q_\alpha}{\partial t} = -ikU_\alpha q_\alpha - ik^3\Sigma\zeta_\alpha, \tag{20c}$$

$$\frac{\partial \zeta_\alpha}{\partial t} = -ikU_\alpha\zeta_\alpha - ik(G_{1\alpha}q_1 + G_{2\alpha}q_2 + G_{\alpha\alpha}q_\alpha), \tag{20d}$$

where $G_{ij} = G(y_i, y_j)$. In a matrix form, Eq. (20) become

$$\dot{\boldsymbol{\xi}} = \boldsymbol{M}\boldsymbol{\xi}, \quad \boldsymbol{\xi} = \begin{bmatrix} q_1 \\ q_2 \\ q_\alpha \\ \zeta_\alpha \end{bmatrix}, \quad \text{and} \tag{21}$$

$$\boldsymbol{M} = -ik \begin{bmatrix} (1+\Lambda) - mG_{11} & -mG_{12} & -mG_{1\alpha} & 0 \\ mG_{12} & (1-\Lambda) + mG_{22} & mG_{2\alpha} & 0 \\ 0 & 0 & U_\alpha & k^2\Sigma \\ G_{1\alpha} & G_{2\alpha} & G_{\alpha\alpha} & U_\alpha \end{bmatrix}.$$

The solutions of (21) are the normal modes of the system which can be also obtained in a more standard way using matching conditions at the interfaces (see the Appendix). Nonetheless, the representation of the solution in the form of (20) provides mechanistic interpretation of the normal mode instability in terms of the interfacial vorticity waves which interact in a distance. Furthermore, the vorticity and displacement perturbations (q_α, ζ_α) can be decomposed into the vorticity of the pro- and counter-propagating capillary waves (q_α^+, q_α^-) using Eq. (15). Hence, after applying a similarity transformation, one can transform (21) to the dynamic equation set for the four vorticity waves,

$$\dot{\boldsymbol{q}} = \tilde{\boldsymbol{M}}\boldsymbol{q}, \tag{22}$$

where $\boldsymbol{q} = \begin{bmatrix} q_1 \\ q_2 \\ q_\alpha^+ \\ q_\alpha^- \end{bmatrix}$ and

$$\tilde{\boldsymbol{M}} = -ik \begin{pmatrix} (U_1 - G_{11}m) & -G_{12}m & -mG_{1\alpha} & -mG_{1\alpha} \\ G_{12}m & (U_2 + G_{22}m) & mG_{2\alpha} & mG_{2\alpha} \\ \dfrac{G_{1\alpha}}{2}\sqrt{\dfrac{\Sigma k^2}{G_{\alpha\alpha}}} & \dfrac{G_{2\alpha}}{2}\sqrt{\dfrac{\Sigma k^2}{G_{\alpha\alpha}}} & U_\alpha + \sqrt{G_{\alpha\alpha}\Sigma k^2} & 0 \\ -\dfrac{G_{1\alpha}}{2}\sqrt{\dfrac{\Sigma k^2}{G_{\alpha\alpha}}} & -\dfrac{G_{2\alpha}}{2}\sqrt{\dfrac{\Sigma k^2}{G_{\alpha\alpha}}} & 0 & U_\alpha - \sqrt{G_{\alpha\alpha}\Sigma k^2} \end{pmatrix}.$$

The off-diagonal terms of $\tilde{\boldsymbol{M}}$ represent the interaction between the waves which affect their propagation rate and growth. The diagonal entries represent the phase speeds of each wave in isolation, which are composed of the self propagation speed of each wave and the advection by the flow at the location of the wave. The upper-left 2×2 subsystem characterizes the interacting Rossby waves in absence of capillary waves. As revealed by Heifetz *et al.*,[7] for an unbounded shear layer or by Biancofiore and Gallaire[8] for the present wake configuration, the two Rossby waves interact in a way to produce shear instability through the asymmetric coupling terms $\pm mG_{12}$. Since G_{12} scales like $1/k$ for $k > 1$, the self counter-propagating speed of the Rossby waves decreases with wavenumber, approximately as k^{-1}, as shown in Figure 2(b), in contrast to the self propagation speed of the capillary waves, which *increases* with the wavenumber approximately as $k^{1/2}$. From this perspective, capillary waves differ fundamentally from Rossby and gravity waves (the latter has a propagation rate proportional to $k^{-1/2}$, see Umurhan and Heifetz[13]).

IV. TEMPORAL STABILITY ANALYSIS

In this section, we present the temporal stability analysis of the normal modes in terms of the interacting vorticity waves. We first focus on the influence of the surface tension on the modes (Subsection IV A) and then discuss (Subsection IV B) which interacting waves are forming the unstable modes. Finally (Sec. IV C), we examine the sensitivity of the instability to the location of the interface.

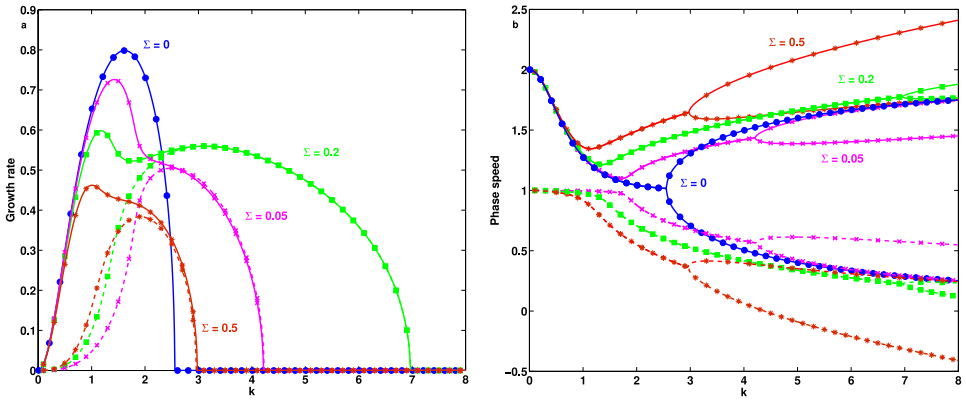

FIG. 3. Growth rate (a) and phase speed (b) versus wavenumber k for different values of the surface tension Σ, $h = 1$, $\Lambda = -1$, $\alpha = 0.5$, and $\delta_w = 0.5$. The circles depict $\Sigma = 0$, the crosses $\Sigma = 0.05$, the squares $\Sigma = 0.2$, and the asterisks $\Sigma = 0.5$. The continuous lines represent the first mode, while the dashed ones the second mode.

A. Influence of the surface tension

The eigenvalues λ of (22) are the normal modes of the system $\lambda_r + i\,\lambda_i$, where λ_r is the growth rate and $c_i = \lambda_i/k$ is the phase speed. Without surface tension ($\Sigma = 0$), only one unstable sinuous mode is found. This mode is created by the interaction of the two counterpropagating RWs and the reader is referred to the previous works[7,8,14] for more details. The growth rate and phase speed of this unstable mode are illustrated by circles in Figure 3 for $h = 1$, $\delta = 0.5$, $\Lambda = -1$, and $\alpha = 0.5$. The growth rate presents a maximum of $\lambda_r = 0.8$ and a cutoff wavenumber of $k = 2.56$. If we introduce the surface tension at the interfaces, a second unstable mode appears. The maximal growth rate of the first mode is damped, but the cutoff number significantly increases, until to reach the value of $k = 6.97$ for $\Sigma = 0.2$ (depicted by squares). The second unstable mode concerns large wavenumbers mostly. This agrees with the instability found by Tammisola *et al.*[1] which seems to be characterized by small wavelengths. If we continue to increase the surface tension to $\Sigma = 0.5$, the cutoff wavenumber starts to decrease. Then, the surface tension finally induces a stabilisation. In Fig. 3(b), the phase speeds of the normal modes are illustrated. Interestingly, the mode created by the presence of capillarity propagates at small wavenumbers with the same speed of the interfaces for all the values of Σ, while the other mode, already existing without capillarity propagates with a larger speed. Despite the fact that the chosen geometry is symmetric with respect of the interface ($h = 1$ and $\alpha = 0.5$), a significant asymmetry of the modes with respect of the interface is noticed. This is due to the asymmetric boundary conditions of the sinuous perturbations. When considering the varicose mode instead (not shown here), the phase speeds are completely symmetric with respect of the interfaces for the same set of parameters.

Figure 4 shows the isocontours of the growth rate in the plane Σ-k for the two modes. The maximum of the growth rate for the first mode (a) is in the absence of surface tension, though a local maximum is present at $k = 3.2$ and $\Sigma = 0.16$. The mode induced by the surface tension has a global maximum in correspondence with the local maximum of the first mode. The maximal values of the cutoff wavenumber are included in a range $0.1 < \Sigma < 0.2$. Hence, in this range, capillary effects destabilise the flow most efficiently.

B. Nature of the modes

In Sec. IV A, we have shown a destabilizing influence of the surface tension mainly via the appearance of a second unstable mode in addition to the classical mode associated with the RW-interaction. These modes can be obtained as well in a more traditional way by using matching conditions at the interfaces (see the Appendix for completeness). Here, we wish to benefit from the interfacial wave interaction perspective, described in Sec. III, to shed light on the physical interaction mechanisms between the Rossby and capillary waves, where each line in system (22) represents one wave: RW or

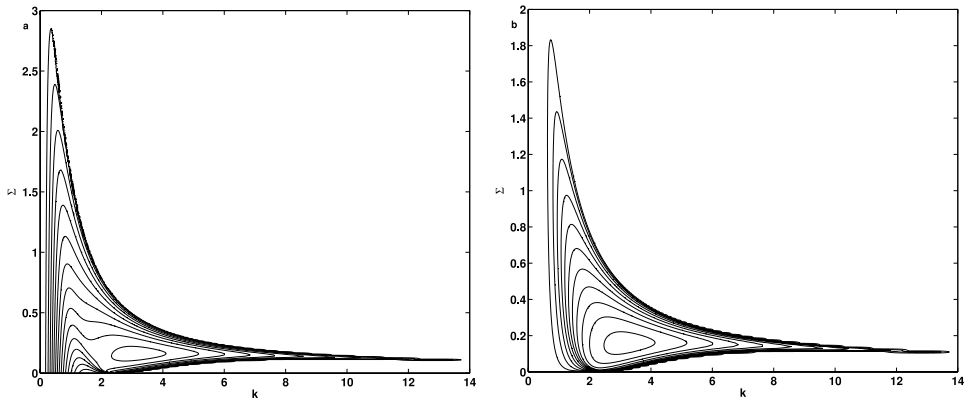

FIG. 4. Contours of the growth rate for the two modes ((a) and (b)) in the plane Σ-k for $h = 1$, $\Lambda = -1$, $\alpha = 0.5$, and $\delta_w = 0.5$. The contours are equally spaced by 0.05.

CW. From now on, we denote $R-$ and $R+$ ($C-$ and $C+$), the Rossby wave (capillary wave) propagating westward and eastward, respectively (see Figure 2).

1. Waves switch off

Starting from the physical system with all four waves (22), we can create other unphysical, but still meaningful systems by "*switching off*" waves. For instance, we can erase the last two lines and columns from the system to recover the dynamical system obtained by Biancofiore and Gallaire[8] (corresponded to the case with $\Sigma = 0$) with the two RWs considered only. To give an example of another partial wave combination, consider the dynamical system corresponding to the coupling of one $R+$ and one $C-$,

$\dot{\boldsymbol{q}}_{1/4} = \tilde{\boldsymbol{M}}_{1/4}\boldsymbol{q}_{1/4}$, with $\boldsymbol{q}_{1/4} = \begin{bmatrix} q_1 \\ q_\alpha^- \end{bmatrix}$ and

$$\tilde{\boldsymbol{M}}_{1/4} = -ik\begin{pmatrix} (U_1 - mG_{11}) & -mG_{1\alpha} \\ -\dfrac{G_{1\alpha}}{2}\sqrt{\dfrac{\Sigma k^2}{G_{\alpha\alpha}}} & U_\alpha - \sqrt{G_{\alpha\alpha}}k\sqrt{\Sigma} \end{pmatrix}.$$

In Figure 5, we show the modal growth rates and phase speeds of these new systems obtained with switching off the waves. While the first mode at small wavenumbers is influenced mainly from the two RWs interaction, at large wavenumbers, the two modes are mainly influenced by the interaction between one RW and one CW propagating in opposite directions (i.e., $R+$ and $C-$; $R-$ and $C+$, depicted by diamonds and squares, respectively). This is because only waves with opposite propagation signs are able to phase-lock in an unstable modal configuration.[15] Simply speaking, waves with positive (negative) correlation between vorticity and displacement propagate to the east (west), with respect to the mean flow. Hence, such two waves with opposite propagation signs can resist the shear and maintain interaction. Furthermore, only waves with opposite propagation signs can mutually reinforce their amplitude by action at a distance and trigger instability. The symmetry between the mode composed of $R+$ and $C-$ and the mode of $R-$ and $C+$ results from the fact that the interface between the immiscible fluids is located just in the middle between the two vorticity jump interfaces (Figure 2). With considering both RWs and one CW (triangles and stars), we have one unstable mode only which approximates the $R+/R-$ interaction at small wavenumbers and the RW-CW interaction at larger wavenumbers. Because systems with waves moving along the same direction are always stable systems with one RW and both CWs present values of the growth rate similar to the $R+/C-$ and $R-/C+$ systems (not shown).

In conclusion, the behaviour of these systems obtained by switching off the waves helps to understand which waves are interacting to create the two modes. At small wavenumbers, the mode is dominated by the $R+/R-$ interaction with a damping effect due to the surface tension, while the

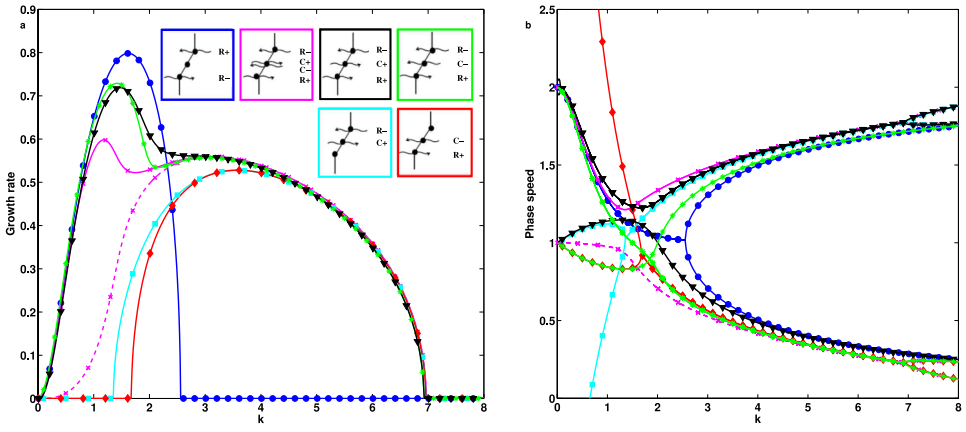

FIG. 5. Growth rate (a) and phase speed (b) versus wavenumber k for $\Sigma = 0.2$, $h = 1$, $\Lambda = -1$, $\alpha = 0.5$, and $\delta_w = 0.5$. The circles depict the unstable mode of the RW-interaction without capillarity effects, the crosses depict the two unstable modes (continuous and dashed line, respectively) due to the 4-waves interaction (Eq. (22)), the stars depict the interaction between the $C-$ and the RWs, the triangles depict the interaction between the $C+$ and the RWs, the squares depict the interaction between the $R-$ and the $C+$, and the diamonds depict the interaction between the $R+$ and the $C-$.

Rossby-capillary interaction dominates the two modes at larger wavenumbers. However, note that these results are for $\alpha = 0.5$. The sensitivity of the results to the location of the capillary interface is explored in Sec. IV C.

2. Amplitudes and phases

For the intermediate regime of wavenumbers, all four vorticity waves may contribute to the modal interaction. The interaction between the vorticity waves can be studied then with observing their amplitudes and the phases. We can obtain amplitudes and phases with computing the eigenvectors V_i of system (22), where the index i depicts a different mode. In particular, the amplitude of each vorticity wave is obtained with $Q_{i,j} = |v_{i,j}|$, where $v_{i,j}$ is the jth component of ith eigenvector, while their normalized phase is $\epsilon_{i,j} = \arg(v_{i,j})/\pi$. We show in Figure 6, the amplitudes ((a) and (b)) and the phases ((c) and (d)) for the two unstable modes with the same set of parameters of Fig. 3. Since surface tension is a small scale phenomenon, generally we expect that it plays a dominant role for large wavenumbers. Indeed, from the gravest mode amplitude decomposition (Figure 6(a)), it is clear that for small wavenumbers, the interaction is mainly between the $R-$ and $R+$ with a phase difference varies from a fully hindering configuration $\Delta\epsilon = 1$ to a full helping configuration $\Delta\epsilon = 0$ with the largest growth rate depicted in the hindering-growing configuration $0.5 < \Delta\epsilon < 1$ (Figure 6(a)). All these are in agreement with previous RW interaction analysis (e.g., Heifetz *et al.*[7]). As the wavenumber increases, the interaction is shifted to a $R-/C+$ one with a locking phase that varies as well with wavenumber from the hindering to the helping regime and a maximal growth rate that is obtained in a growing hindering configuration.

For small and intermediate wavenumbers, the second mode (Figures 6(b) and 6(d)) is a complex combination of the four interfacial waves but this multi-wave interaction results in a small growth rate. For larger wavenumbers, $k > 3$, the growth rates of the two modes practically converge; however, for the second mode, the interaction now is composed of the reciprocal $R+/C-$ configuration. For this large wavenumber regime, the amplitude ratio and the absolute phase difference between the $R+/C-$ in the second mode are practically indistinguishable from the $R-/C+$ of the first mode.

C. Location of the interfaces

In this section, we wish to analyze the dependence of the two unstable modes on the position of the interfaces. The choice of $\alpha = 0.5$ settles the CWs exactly in the middle between the two counter-propagating RWs. We may expect at first sight that if the interface is closer to the southern (northern) edge, the interaction will be dominated by the $R+/C-$ ($R-/C+$) pairs.

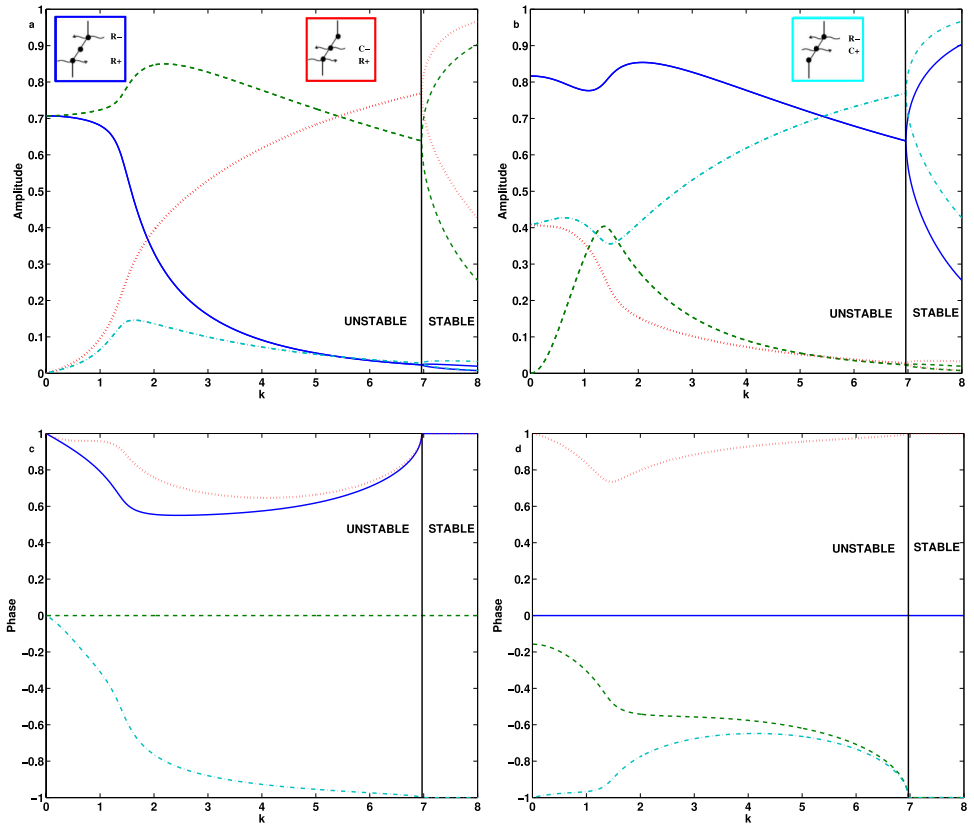

FIG. 6. Amplitudes ((a) and (b)) and phases ((c) and (d)) for the component of the eigenvectors of the system in Eq. (22) for $\Sigma = 0.2$, $h = 1$, $\Lambda = -1$, $\alpha = 0.5$, and $\delta_w = 0.5$. The continuous line depicts the first component ($R+$), the dashed line depicts the second component ($R-$), the dotted one depicts the third component ($C+$), and the dashed-and-dotted line depicts the fourth component ($C-$).

In Figure 7, we illustrate the growth rate (a) and phase speed (b) with choosing three different values of α: $\alpha = 0.3$, $\alpha = 0.5$, and $\alpha = 0.7$. All other parameters are kept constant: $\Sigma = 0.2$, $h = 1$, $\Lambda = -1$, and $\delta_w = 0.5$. The growth rates of $\alpha = 0.3$ and $\alpha = 0.7$ are practically equal, while the phase speeds of the second mode are symmetric with respect to the velocity of the interface ($U_\alpha = 1$).

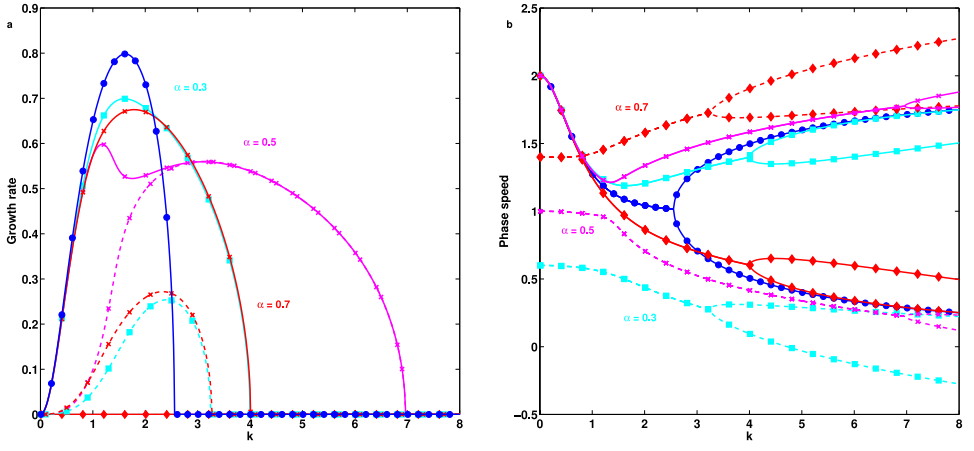

FIG. 7. Growth rate (a) and phase speed (b) versus wavenumber k for different values of the parameter α, $\Sigma = 0.2$, $h = 1$, $\Lambda = -1$, and $\delta_w = 0.5$. The squares depict $\alpha = 0.3$, the crosses $\alpha = 0.5$, the asterisks depict $\alpha = 0.7$, and the circles depict the $R+/R-$ interaction. The continuous lines represent the first mode, while the dashed ones the second mode.

Moreover, the first mode now seems to be completely independent on the second one. Its maximum growth rate is larger than the one of $\alpha = 0.5$, but its cutoff number decreases. However, the cutoff number is still larger than the case without surface tension ($R+/R-$ interaction, circles). On the other hand, both the growth rate and the cutoff number of the second mode are significantly damped when moving the interface closer to the northern/southern edge. Hence, decreasing the distance between the capillary interfaces to one of the edges of the shear layer has an ambiguous effect. It seems to increase the instability of the first mode, probably because the distant interaction between the capillary and the Rossby waves becomes more efficient, but it has the opposite effect on the second mode.

To investigate further this subtle behaviour, we analyse again the respective amplitudes of the capillary and Rossby waves (the phases are omitted for conciseness) as done in Sec. IV B. The amplitudes of the four waves contributing to the two eigenmodes for $\alpha = 0.3$ and $\Sigma = 0.2$ are represented in Figures 8(a) and 8(b). It is seen that the first and most unstable mode (represented in Figure 7 as a continuous line) is made of the RW pair at small wavenumber with the $R+$ progressively diminishing in favor of the $C+$ as the wavenumber increases and reaches k_{max} associated to the maximum growth-rate. Therefore, it appears that the most destabilizing interaction results from a CW riding on the interface locking with the counterpropagating RW sitting on the farthest edge from the interface. For $\alpha = 0.3$, the $R-$ sitting on the northern edge interacts with the $C+$ riding on the interface. In contrast, the second less unstable mode has important contributions from the $R+$ and the $C-$. A detailed inspection of synthetic wave combinations (as those depicted in Figure 5) shows however that this dual interaction is not sufficient and that the coupling with the additional capillary wave ($C+$ in this case) is a prerequisite for instability.

This scenario is fully corroborated by the analysis of Figures 8(c) and 8(d), which demonstrates that for an interface located above the equator, for instance, for $\alpha = 0.7$, the southern edge wave,

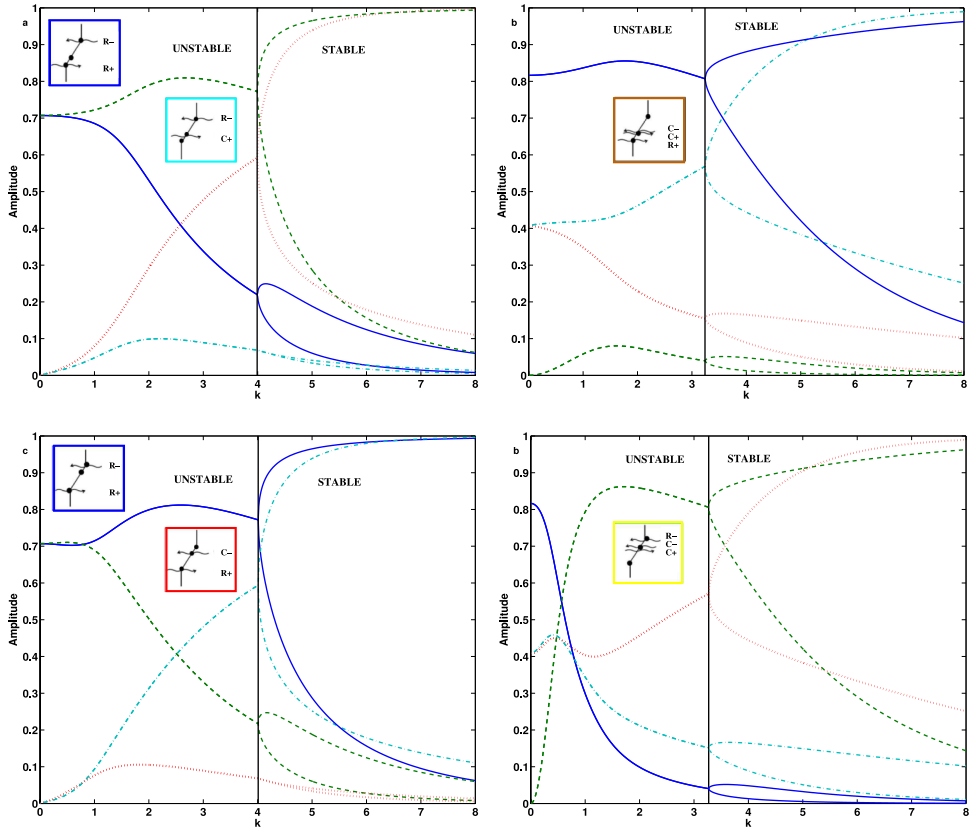

FIG. 8. Amplitudes ((a) and (b)) for the component of the eigenvectors of the system in Eq. (22) for $\Sigma = 0.2$, $h = 1$, $\Lambda = -1$, $\delta_w = 0.5$, and ((a) and (b)) $\alpha = 0.3$ and ((c) and (d)) $\alpha = 0.7$. The legend is the same of Fig. 6.

i.e., the $R+$ locks in with the $C-$ sitting on the interface to yield the strongest interaction. Figure 8 therefore highlights the strong contribution of the pair $R-/C+$ (respectively, $R+/C-$) for $\alpha = 0.3$ (respectively, $\alpha = 0.7$): for wavenumbers close to maximum growth, the main instability results from the coupling of a CW active on the interface with the RW riding on the farthest edge. In this regime, where surface tension has an overall stabilizing influence (in terms of maximum growth-rate), the shift from a RW to a CW in the dominant pair of waves will be seen to have a major influence onto the spatio-temporal behavior of the wake, as further explained in Sec. V.

Finally, we illustrate in Figure 9, the phase speeds of the waves in isolation (i.e., the terms in the brackets of the diagonal entries of the matrix $\tilde{\boldsymbol{M}}$ in Eq. (22)) as a function of the wavenumber k are depicted in Fig. 9 for three different values of surface tension $\Sigma = (0.05, 0.2, 0.5)$ for two interfacial positions $\alpha = (0.3, 0.7)$ in complement to $\alpha = 0.5$ depicted in Figure 2(b). The velocity ratio is $\Lambda = -1$ so that the "homebase" mean flow velocity of the $R-$ is $U_2 = 2$ and of the $R+$ is $U_1 = 0$. The plot confirms that the self counter-propagating speed of the Rossby waves decreases with wavenumber, approximately as k^{-1}, while the self propagation speed of the CWs increases with the wavenumber approximately as $k^{1/2}$, see Sec. III B. The more similar is the phase speed (self plus mean flow advection) between the waves, which is the easier for them to phase-lock in a growing configuration. Hence, Figure 9 confirms that the instability at small and intermediate wavenumbers results from different combinations of interactions between RWs and CWs. For larger wavenumbers, the presence of surface tension allows new modes of unstable interaction between $R+/C-$ and $R-/C+$, and this explains the counterintuitive effect of destabilization by surface tension. This is the essence of the counterintuitive effect of destabilization by surface tension. Note also that when the interface is not located right in between the two mean vorticity jumps, the different dependence of self-propagation speed between the RW and CW originates in the unstable interaction at large wavenumbers between $R+/C-$ (for $\alpha = 0.7$) and $R-/C+$ (for $\alpha = 0.3$). This means that the CW counterintuitively interacts with the RW at the farther edge rather than with the RW located on its nearest edge.

In conclusion, the square-root dependence of the capillary wave phase velocity with the wavenumber (as shown in Figures 2(b) and 9) is the main reason for this counterintuitive interaction. Since the self propagation speed of the CWs increases with wavenumber, at large wavenumbers, they counter propagate too fast to phase lock with their adjacent RW whose self propagation rate decreases with the wavenumber. Hence, a larger shear difference between the CW and the RW is required to enable phase locking between the two. This is achieved when the CW interacts with the RW of its farthest edge.

V. SPATIO-TEMPORAL INSTABILITY ANALYSIS BY MEANS OF IMPULSE RESPONSE

In order to investigate the influence of surface tension on the spatio-temporal properties of shear flows, we now determine the absolute/convective properties of the model wake flow investigated in

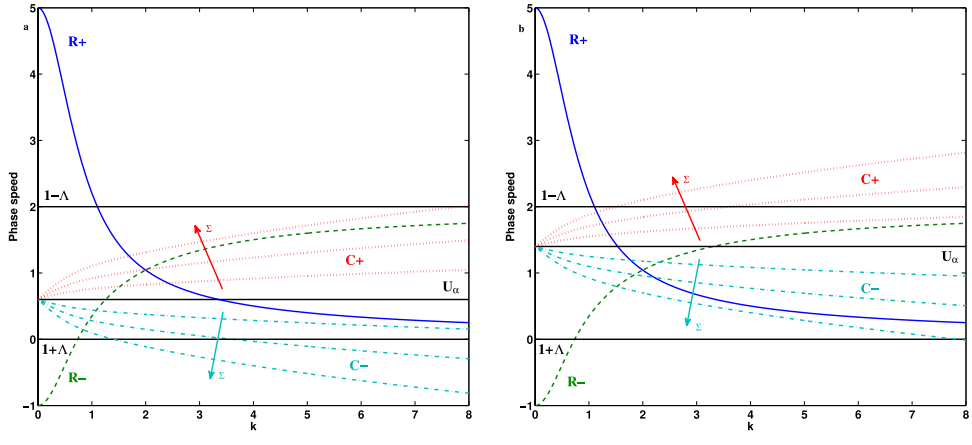

FIG. 9. Phase speeds of the wave in isolation for $h = 1$, $\Lambda = -1$, $\delta_w = 0.5$, and (a) $\alpha = 0.3$, (b) $\alpha = 0.7$. We have traced the curves for three different values of the surface tension $\Sigma = (0.05, 0.2, 0.5)$. The continuous line depicts $R+$, the dashed line depicts $R-$, the dotted one depicts $C+$, and the dashed-and-dotted line depicts $C-$.

this work. An alternative to the classical method which consists in determining the most unstable admissible k^+/k^- saddle point in the complex wave number plane, as made by Biancofiore and Gallaire,[16] for instance, we resort here to the direct computation of the impulse response. For this purpose, we approximate the spatially localized Dirac function serving as an initial condition by a surrogate peaked Gaussian distribution consisting of the superimposition of N_k wavenumbers ($k_j = j\delta k$) equally sampled at δk resolution ($k_j = j\delta k$) and with amplitude A_j and vorticity weighted according to the eigenmodes $X_p(k_j)$ associated to the eigenvalues $\lambda_p(k_j)$. The initial condition thereby writes

$$\mathbf{X(0)} = \sum_{\mathbf{j=1}}^{\mathbf{N_k}} \sum_{\mathbf{p=1}}^{\mathbf{4}} \mathbf{A_j X_p(k_j)} \exp^{\mathbf{i(k_j x)}} \tag{23}$$

and evolves according to

$$\mathbf{X(t)} = \sum_{\mathbf{j=1}}^{\mathbf{N_k}} \sum_{\mathbf{p=1}}^{\mathbf{4}} \mathbf{A_j X_p(k_j)} \exp^{\mathbf{i(k_j x - \lambda_p(k_j) t)}}. \tag{24}$$

The number of Fourier modes N_k has to be chosen large enough to result in a sufficient spatial resolution of the wavepacket, since $\delta x = 2\pi/(k_{max})$ with $k_{max} = N_k \delta k$. The wavenumber resolution δk has also to be chosen carefully to ensure that the spatial expansion of the wavepacket can be captured at sufficient evolved time horizons, as the maximum domain size L_x before the periodicity starts to mix the trailing and receding edges is given by $L_x = \frac{1}{2\pi\delta k}$. We have verified that the following values $N_k = 12\,500$ and $\delta k = 0.002$ are sufficient to capture the wavepacket evolution in the limit of the machine accuracy. The wavepacket amplitude is subsequently extracted using a Hilbert transform.[17]

Typical results are shown in Figure 10. In each case, the demodulated wavepacket amplitude is first premultiplied by $\sqrt{t}$, so as to match the asymptotic long time expression of the impulse response, as given by Huerre and Monkewitz.[18] Such an algebraic correction was included in Gallaire and

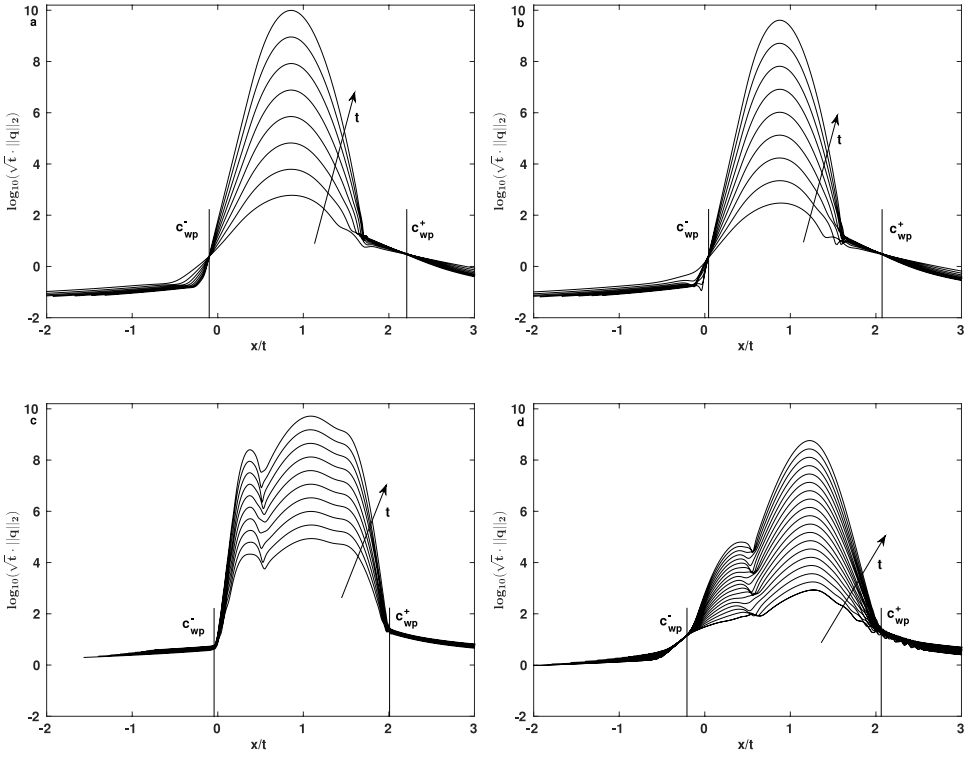

FIG. 10. The spatio-temporal spreading of the enstrophy ($\sqrt{t}\cdot\|q\|_2$) for the 4-wave system for $h = 1$, $\alpha = 0.5$, $\delta_w = 0.5$, (a) $\Lambda = -0.75$, $\Sigma = 0$, (b) $\Lambda = -0.65$, $\Sigma = 0$, (c) $\Lambda = -0.65$, $\Sigma = 0.2$, and (d) $\Lambda = -0.65$, $\Sigma = 0.5$. The group velocities of front and of the back of the wavepacket are marked by c^-_{wp} and c^+_{wp}, respectively.

Chomaz[19] to retrieve A/C transition curves: it is useful because the numerical estimation of the impulse response is limited to a finite time interval because of the finite precision arithmetic. This premultiplicated wavepacket amplitude is then plotted as a function of the ray velocity x/t in Figure 10. Figures 10(a) and 10(b) are obtained in absence of surface tension for two values of Λ. For a rather large value of $\Lambda = -0.75$ (a), the advection is weak and the wavepacket is seen to invade the entire domain. While the leading edge and the summit of the wavepacket are travelling downstream, the trailing (or receding) edge of the wavepacket propagates upstream: the instability is absolute. In contrast, for a larger value of the velocity ratio $\Lambda = -0.65$, the growth of the instability is not strong enough to withstand the advection and the trailing (or receding) edge of the wavepacket also propagates downstream, pointing to a convective instability.

While in the absence of surface tension, the wavepacket has the usual bell shape, the addition of a finite amount of surface tension changes the wavepacket shape as well as the propagation direction of the edges of the packet, similarly to what noticed by Rees and Juniper[20] for a top-hat jet/wake profile. Observe in Figures 10(c) and 10(d) that the instability becomes absolute while the wavepacket splits in two. This type of double-headed wavepacket suggests that the two unstable branches give rise to two different wavepackets that overlap in the central region, as will be assessed next. It also demonstrates the large influence of surface tension on the spatio-temporal stability properties of the wake: adding a progressive amount of surface tension first makes the flow more absolutely unstable before it eventually increases the convective character of the instability. This is best seen in Figure 11 where the velocity of the trailing edge of the wavepacket is plotted as a function of Σ for $\Lambda = -0.65$. Observe also that the destabilizing effect of the surface tension is seen to depend on the exact location of the interface. When the interface is located in the high velocity region ($\alpha > 0.5$), the addition of surface tension does surprisingly suffice to withstand the advection. In contrast, the more the interface penetrates into the low velocity region associated to the inner wake ($\alpha > 0.5$), the more the instability is overwhelmed by the advection. In brief, we are left with the following apparent paradox: wakes where the immiscible interface is relatively slow ($\alpha < 0.5$) are convectively unstable, while wakes where the interface is relatively fast ($\alpha > 0.5$) tend to become absolutely unstable.

This counterintuitive observation can be interpreted by considering the coupling of a counterpropagating pair of waves consisting of the combination of a Rossby wave and a capillary wave. As described in Sec. IV B, when $\alpha < 0.5$ and surface tension is sufficient (typically $\Sigma > 0.1$), an unstable

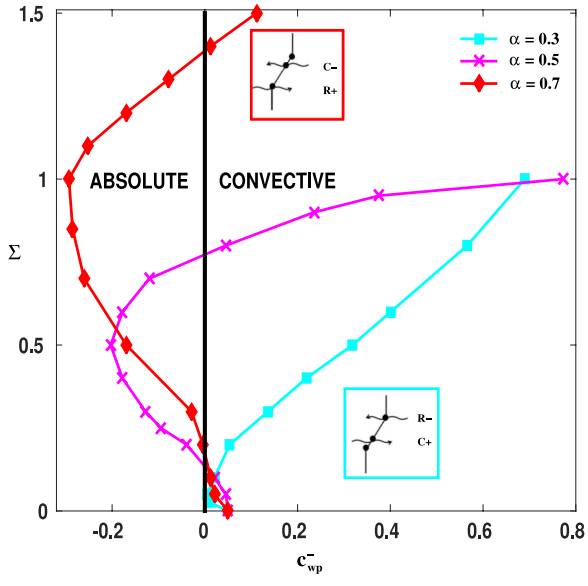

FIG. 11. The group velocity of the back of the wavepacket c_{wp}^- depending on the surface tension Σ with $\delta_w = 0.5$, $h = 1$ and $\Lambda = -0.65$. Three different positions of the interface are depicted: $\alpha = 0.3$ (squares), $\alpha = 0.5$ (crosses), and $\alpha = 0.7$ (asterisks).

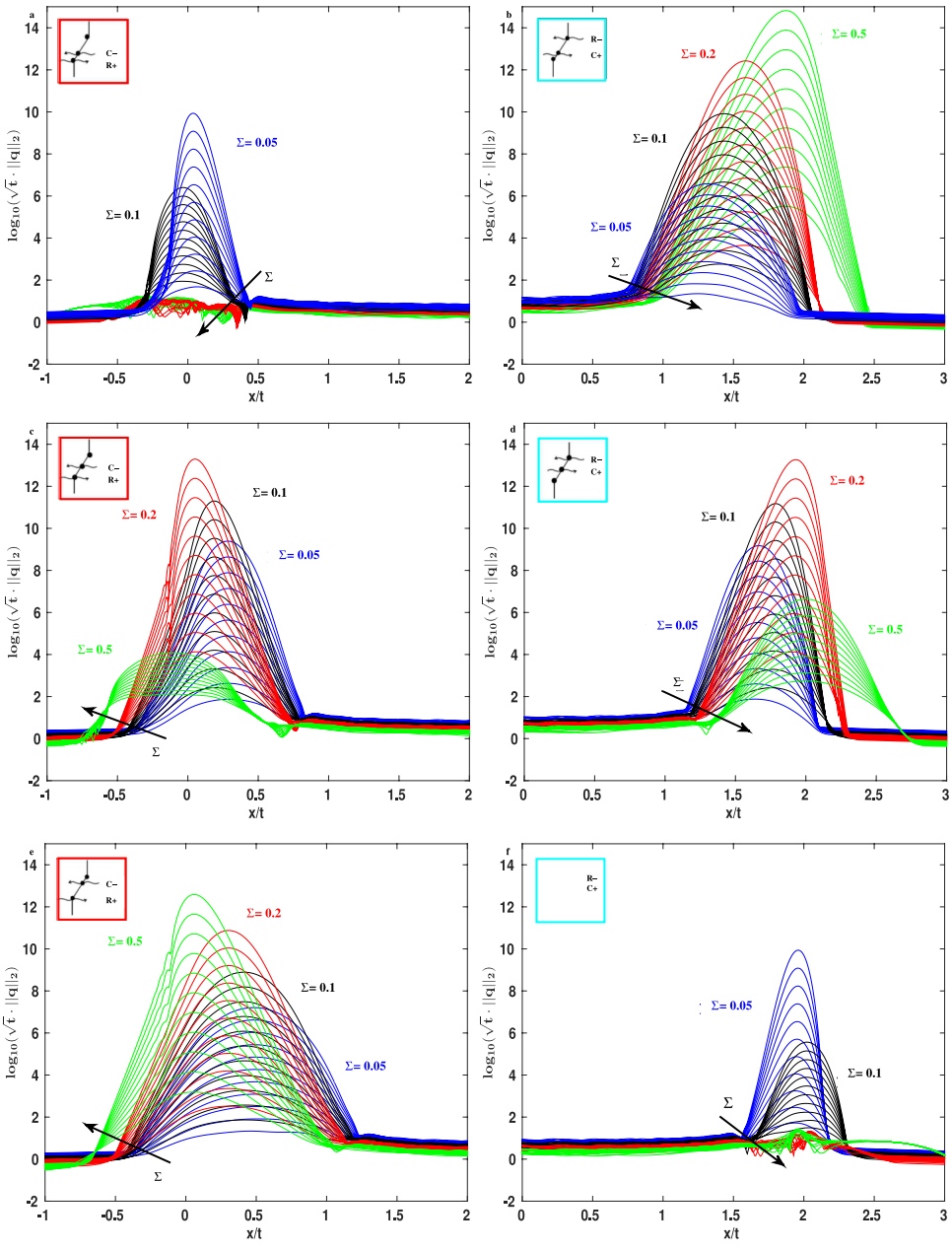

FIG. 12. The spatio-temporal spreading of the enstrophy ($\sqrt{t}\cdot\|q\|_2$) with varying the value of the surface tension Σ for the systems with (a), (c), (e) $R+$ plus $C-$ and (b), (d), (f) $R-$ plus $C+$ for $h=1$, $\Lambda=-1$, $\delta_w=0.5$ for (a), (b) $\alpha=0.3$, (c), (d) $\alpha=0.5$, and (e), (f) $\alpha=0.7$. The blue line depicts $\Sigma=0.05$, the black line $\Sigma=0.1$, the red line $\Sigma=0.2$, and the green line $\Sigma=0.5$.

pair is made of an $R-$ and a $C+$, while when $\alpha > 0.5$, it is made of an $R+$ and a $C-$, i.e., in both situations, a capillary wave locks in with a Rossby wave riding on the farthest edge from the interface. The artificially separated wavepackets resulting from the separate development of these two pairs of waves are represented in Figure 12(a), 12(c), 12(e) and 12(b), 12(d), 12(f). We observe that the synthetic $R-/C+$ wavepacket is indeed unstable (respectively, stable) when $\alpha = 0.3$ (respectively, $\alpha = 0.7$) as seen in Figure 12(b) (respectively, 12(f)). In contradistinction, the synthetic $R+/C-$ wavepacket is stable (respectively, unstable) when $\alpha = 0.3$ (respectively, $\alpha = 0.7$) as seen in Figure 12(a) (respectively, 12(e)). For a centered interface $\alpha = 0.5$ (see Figs. 12(c) and 12(d)), both synthetic wavepackets are unstable, as suggested by Figure 5(a).

As sketched in the insets of Figure 12, it can be inferred by considering the mean advection velocity of its constitutive waves that the $R-/C+$ pair is affected by a larger advection than the $R+/C-$ pair. This results in the absolute character of the instability being reinforced when the latter pair is favoured, i.e., for a finite amount of surface tension and for $\alpha = 0.7$ (Figures 11 and 12(c)), i.e., counterintuitively for a relatively fast interface. In contrast, when the interface is located in the slow inner region of the wake, for instance, for $\alpha = 0.3$, the $R-/C+$ pair is favoured, which benefits from a large advection, reinforcing the convective character of the instability (Figures 11 and 12(b)).

This argumentation can be further justified by following the analysis of Biancofiore and Gallaire,[8] who have explained the enhancement of the absolutely unstable nature of wake flows through the addition of a moderate confinement[23] by examining the average group velocity of the two RWs, taken in isolation. They have noticed a remarkable correspondence between the absolute/convective transition and the average group velocity, which suggests that the enhancement of absolute instability triggered by the confinement is mainly due to the dependence on the confinement of the group velocity of the counterpropagating RWs taken freely to propagate, without interacting one with each other. Since the slow $R+/C-$ pair is favoured by an interface located above the equator (typically for $\alpha = 0.7$), while in contrast, the fast $R-/C+$ pair dominates for interfaces located below the equator (typically for $\alpha = 0.3$), and since the resulting growth-rate is very similar for both interface locations, the difference in mean average group velocity between these two pairs results in the absolute character of the instability when $\alpha = 0.7$ and the reinforcement of the convective character of the instability when $\alpha = 0.3$, accounting for the observations of Figure 11.

When the surface tension is further increased, the interplay between the mean advection of the waves, well characterized by the mean group velocity of the interacting waves taken in isolation (Figure 13), and the reduced growth of the instability associated to a shift towards small k of the unstable wavenumber band (Figure 4), results in an overall stabilization with the tendency towards absolute instability of the $R+/C-$ pair being progressively overcome by the domination of the $R-$ which replaces the $C-$ in the shrinking unstable wavenumber range. This leads to a local minimum of the receding wavepacket edge velocity located around $\Sigma = 1$ in Figure 11.

The RW/CW interpretation therefore enables to unravel the mechanism behind the significant reinforcement of the absolute instability by a finite amount of surface tension when $\alpha > 0.5$. As the surface tension increases to order one values, the $R+$ progressively couples with the $C-$ which both combine into an unstable but slowly advecting instability mode, since the constitutive pair is centered around the low velocity region of the inner wake.

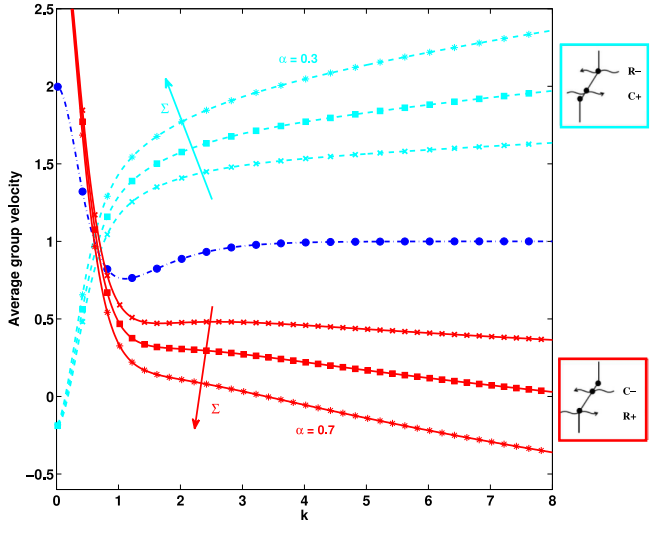

FIG. 13. The average group velocity of the (i) two RWs (dashed-and-dotted line), (ii) $R-$ and $C+$ with $\alpha = 0.3$ (dashed lines), and (iii) $R+$ and $C-$ with $\alpha = 0.7$ (continuous lines) for different values of Σ, $\delta_w = 0.5$, $h = 1$, and $\Lambda = -1$. Crosses depict $\Sigma = 0.05$, squares depict $\Sigma = 0.2$, and asterisks depict $\Sigma = 0, 5$. Note that the group velocities of the RWs do not depend on either the surface tension or the location of the interface.

VI. CONCLUSIONS

In this paper, we have modeled a wake with a piecewise broken line profile, in order to be able to describe the system by means of an interfacial wave interaction perspective. This perspective has been already used to explain geophysical flows systems,[7,14] including possibly buoyancy effects.[9,10,13] In this manner, we have explained the counterintuitive destabilization noticed first by Tammisola *et al.*[1] in a wake of two immiscible flows. This destabilization is due to the presence of a new unstable mode created by a Rossby-capillary waves interaction. Moreover, the absolute nature of the instability of the Rossby-capillary mode increases in the presence of a moderate surface tension. This is caused by the influence of the surface tension on the waves, responsible for the dominating instability, taken in isolation.

In particular, we have found that the surface tension associated with the immiscible interface creates two capillary waves at riding on the interface which propagate in opposite directions, when viewed in the reference frame traveling at the velocity of the interface. These waves can interact with the RWs created at the edges where the potential vorticity is discontinuous. Interestingly, the propagation rate of capillary waves increases with wavenumber (roughly as $k^{1/2}$) in contradistinction of interfacial Rossby waves and gravity waves[13] whose propagation rates decrease with wavenumber (roughly as k^{-1} and $k^{-1/2}$, respectively).

By means of a temporal analysis, we have found that the interaction between one RW and one CW, which is propagating in opposite direction creates a second unstable mode in addition to the mode created by the RW-interaction typical of wakes.[8] This interaction was confirmed also by studying the amplitudes and the phases of the vorticity waves. The maximum growth rate and the cutoff wavenumber were found to be significantly depending on the position of the interfaces. If the interface is located close to the northern (southern) edge, the interaction between the $R-$ and $C+$ ($R+$ and $C-$) is favored at large wavenumbers and rather weak surface tension, while it is the opposite at larger surface tension and small wavenumbers. This counterintuitive interaction between a CW and the farthest RW is due to the anomalous growing evolution of the CW-propagation rate with the wavenumber. This leads to a phase locking between capillary and Rossby waves in a far distance, since then the shear between the waves manages to balance the large counterpropagation speed of the CWs.

Furthermore, we have conducted a spatio-temporal analysis by means of an impulse response to a localized perturbation of the dynamical system describing the four waves (two RWs and two CWs). We have noticed that the absolute unstable character of the wakes is significantly enhanced if the location of the interface is close to the northern edge, i.e., the fastest edge. This is counter-intuitive since this situation corresponds to a relatively fast interface, which could have been thought at first sight to reinforce the convective character of the instability. We have explained this apparent paradox with noticing that the mean average group velocity of the waves dominating the instability at $\alpha = 0.7$, i.e., $R-/C+$, decreases with the surface tensions.

While this paper is dedicated to wakes, this type of analysis can be easily conducted for other shear flows, such as jets or mixing layer. Tammisola *et al.*[2] have shown, for instance, that also planar jets can be destabilized by surface tension. While for the temporal stability, mixing layers and jets should have a qualitative behaviour similar to wakes, the spatio-temporal evolution could present significant discrepancies. For jets, the most favorable location of the interfaces for absolute instability should differ with the respect to wakes.

The wave-coupling mechanism investigated in this study can be related to other instabilities due to interacting waves such as Holmboe modes[12] or the Taylor[21]-Caulfield[11] instability. Capillary waves behave similarly to gravity waves generated by stratification. It would be therefore worthwhile to study the spatio-temporal evolution of instabilities caused by stratification by means of an impulse response as made in Sec. V. Finally, aerosol spraying from the ocean to the atmospheric boundary layer results from small scale capillary water waves, where both buoyancy and surface tension play a role. Hence, the present work may constitute a starting point for studies devoted to understanding the evolution and interaction of these waves from an action at a distance perspective.

ACKNOWLEDGMENTS

The support of ERCOFTAC Leonhard Euler pilot center is acknowledged.

APPENDIX: NORMAL MODE PERSPECTIVE: DISPERSION RELATIONS

In this section, we obtain the "classical" dispersion relation (see chapter 8 of Drazin and Reid[22]) associated to the model described in Sec. II A.

It is possible to linearize the non-dimensional incompressible 2D Euler's equations about the base flow U assuming small perturbations on the flow,

$$ik(U-\frac{\omega}{k})\tilde{u}+\frac{dU}{dy}\tilde{v}+ik\tilde{p}=0, \tag{A1a}$$

$$ik(U-\frac{\omega}{k})\tilde{v}+\frac{d\tilde{p}}{dy}=0, \tag{A1b}$$

$$ik\tilde{u}+\frac{d\tilde{v}}{dx}=0, \tag{A1c}$$

where we have introduced the classic normal mode decomposition: for a generic quantity, $\hat{a}$ derives from the decomposition in normal modes $a'=\tilde{a}(y)\exp^{i(kx-\omega t)}$. Note that k and ω are taken dimensionless by means of the set of scale introduced in Sec. II A. At this point, the streamfunction ψ' of the perturbation can conveniently be introduced. Suppose that $u'=\frac{\partial\psi'}{\partial y}$ and $v'=-\frac{\partial\psi'}{\partial x}$ and take also normal modes decomposition $\psi'(x,y,t)=\phi(y)e^{i(kx-\omega t)}$. Therefore, $\tilde{u}=\frac{d\phi}{dy}$ and $\tilde{v}=-\mathbf{i}k\phi$ are obtained. On using these results into Eq. (A1), the Rayleigh stability equation is obtained as follows:

$$(U-\frac{\omega}{k})(\frac{d^2\phi}{dy^2}-k^2\phi)-\frac{d^2U}{dy^2}\phi=0. \tag{A2}$$

Observe in Fig. 1 that the flow could be divided in seven sub-domains, separated by $y=h_1\pm\frac{\delta_w^*}{2}$, where the vorticity has a discontinuity, and by the interfaces $y=\pm y_\alpha$. The total streamfunction can be decomposed into basic and perturbation contributions,

$$\Psi_i(x,y,t)=U_i y+\phi_i(y)\cdot e^{i(kx-\omega t)}, \tag{A3}$$

with i = 1,...,7. Since $U_i''(y)=0$ for each sub-domain i, the solution of Rayleigh equation degenerates in an harmonic solution $\phi_i=A_ie^{ky}+B_ie^{-ky}$, yielding 14 unknowns ($A_i$, B_i). We can divide between sinuous and varicose perturbations by taking advantage of the symmetry of the domain, so the fourteen unknowns reduce to seven. Further constraints are to be imposed with considering only one half of the model: imposition of zero y-velocity at the wall, continuity of the particle displacement and of the pressure (excluding where the surface tension is present) on the interfaces between sub-domains. Thus, the equations of motion and the boundary conditions are reduced to a single relationship between the frequency ω, the wavenumber k, and the parameters of the model $(U_j,\rho_j,h_j,\delta_w^*,\alpha,\sigma)$. The dispersion relation can only be satisfied for certain eigenvalues, (ω, k), from which corresponding eigenfunctions, $\phi_i(y)$, can be calculated. The dimensionless varicose and sinuous dispersion relations, so, are as follows:

$$D\equiv(1-S)\frac{M_2-\tanh[k\delta_w(1-\alpha)]}{1-M_2\tanh[k\delta_w(1-\alpha)]}-(1+S)\frac{[M_1-\tanh(k\delta_w\alpha)]}{[1+M_1\tanh(k\delta_w\alpha)]}+$$
$$+\frac{4S\Lambda}{k\delta_w[1+\Lambda(1-2\alpha)-\frac{\omega}{k}]}+\frac{k\Sigma}{[1+\Lambda(1-2\alpha)-\frac{\omega}{k}]^2}=0, \tag{A4}$$

$$D\equiv(1-S)\frac{N_2-\tanh[k\delta_w(1-\alpha)]}{1-N_2^*\tanh[k\delta_w(1-\alpha)]}-(1+S)\frac{[N_1-\tanh(k\delta_w\alpha)]}{[1+N_1\tanh(k\delta_w\alpha)]}$$
$$+\frac{4S\Lambda}{k\delta_w[1+\Lambda(1-2\alpha)-\frac{\omega}{k}]}+\frac{k\Sigma}{[1+\Lambda(1-2\alpha)-\frac{\omega}{k}]^2}=0, \tag{A5}$$

where M_1, M_2, N_1, and N_2 are $M_1 = \coth[k(1-\frac{\delta_w}{2})] - \frac{2\Lambda}{k\delta_w(1+\Lambda-\frac{\omega}{k})}$, $M_2 = N_2 = -\coth[k(h-\frac{\delta_w}{2})] - \frac{2\Lambda}{k\delta_w(1-\Lambda-\frac{\omega}{k})}$, and $M_1 = \tanh[k(1-\frac{\delta_w}{2})] - \frac{2\Lambda}{k\delta_w(1+\Lambda-\frac{\omega}{k})}$.

We can construct more simplified models, neglecting the effect of either the surface tension or the shear layer thickness. When Σ is settled to zero, the dispersion relations are straightforward: it is enough to neglect the terms containing the surface tension in Eqs. (A4) and (A5). This particular model has been analyzed by Juniper[24] and Biancofiore and Gallaire,[8,16] and the reader is referred to these publications for the corresponding dispersion relations. When $\delta_w \to 0$, the limit of the non-dimensional dispersion relations becomes

$$D \equiv (1+S)(1+\Lambda-\frac{\omega}{k})^2\coth(k) + (1-S)(1-\Lambda-\frac{\omega}{k})^2\coth(kh) - k\Sigma = 0, \tag{A6}$$

$$D \equiv (1+S)(1+\Lambda-\frac{\omega}{k})^2\tanh(k) + (1-S)(1-\Lambda-\frac{\omega}{k})^2\coth(kh) - k\Sigma = 0, \tag{A7}$$

which are the dispersion relations studied by Rees and Juniper[20] and Biancofiore and Gallaire.[25] The model becomes a top hat jet/wake with the presence of a surface tension on the interfaces. Note that, without shear layer thickness δ_w, the parameter α looses its meaning.

[1] O. Tammisola, F. Lundell, and D. Söderberg, "Effect of surface tension on global modes of confined wake flows," Phys. Fluids **23**, 014108 (2011).
[2] O. Tammisola, F. Lundell, and D. Söderberg, "Surface tension-induced global instability of planar jets and wakes," J. Fluid Mech. **713**, 632-658 (2011).
[3] L. Biancofiore, F. Gallaire, P. Laure, and E. Hachem, "Direct numerical simulations of two-phase immiscible wakes," Fluid Dyn. Res. **46**, 041409 (2014).
[4] F. Lundell, L. D. Söderberg, and P. H. Alfredsson, "Fluid mechanics of papermaking," Annu. Rev. Fluid Mech. **43**, 195-217 (2011).
[5] F. P. Bretherton, "Baroclinic instability and the short wave cutoff in terms of potential vorticity," Q. J. R. Meteorol. Soc. **92**, 335 (1966).
[6] B. J. Hoskins, M. E. McIntyre, and W. Robinson, "On the use and significance of isentropic potential vorticity maps," Q. J. R. Meteorol. Soc. **111**, 877-946 (1985).
[7] E. Heifetz, C. H. Bishop, and P. Alpert, "Counter-propagating Rossby waves in barotropic Rayleigh model of shear instability," Q. J. R. Meteorol. Soc. **125**, 2835-2853 (1999).
[8] L. Biancofiore and F. Gallaire, "Counterpropagating Rossby waves in confined plane wakes," Phys. Fluids **24**, 074102 (2012).
[9] N. Harnik, E. Heifetz, O. M. Umurhan, and F. Lott, "A buoyancy-vorticity wave interaction approach to stratified shear flow," J. Atmos. Sci. **65**, 2615-2630 (2008).
[10] A. Rabinovich, O. M. Umurhan, N. Harnik, F. Lott, and E. Heifetz, "Vorticity inversion and action-at-a-distance instability in stably stratified shear flow," J. Fluid Mech. **670**, 301-325 (2011).
[11] C. P. Caulfield, "On the behaviour of symmetric waves in stratified shear layers," J. Fluid Mech. **258**, 255-285 (1994).
[12] J. Holmboe, "On the behaviour of symmetric waves in stratified shear layers," Geophys. Publ. **24**, 67-113 (1962).
[13] O. M. Umurhan and E. Heifetz, "Holmboe modes revisited," Phys. Fluids **19**, 064102 (2007).
[14] E. Heifetz and J. Methven, "Relating optimal growth to counterpropagating Rossby waves in shear instability," Phys. Fluids **17**, 064107 (2005).
[15] E. Heifetz, C. H. Bishop, B. J. Hosking, and J. Methven, "The counter-propagating Rossby-wave perspective on baroclinic instability. I: Mathematical basis," Q. J. R. Meteorol. Soc. **130**, 211-231 (2004).
[16] L. Biancofiore and F. Gallaire, "Influence of shear layer thickness on the stability of confined two-dimensional wakes," Phys. Fluids **23**, 034103 (2011).
[17] I. Delbende, J. M. Chomaz, and P. Huerre, "Absolute/convective instabilities in the Batchelor vortex: A numerical study of the linear impulse response," J. Fluid Mech. **335**, 229-254 (1998).
[18] P. Huerre and P. A. Monkewitz, "Absolute and convective instabilities in free shear layer," J. Fluid Mech. **159**, 151-168 (1985).
[19] F. Gallaire and J.-M. Chomaz, "Mode selection in swirling jet experiments: A linear stability analysis," J. Fluid Mech. **494**, 223-253 (2003).
[20] S. J. Rees and M. P. Juniper, "The effect of surface tension on the stability of unconfined and confined planar jets and wakes," J. Fluid Mech. **633**, 71-97 (2009).
[21] G. J. Taylor, "Effect of variation in density on the stability of superposed streams of fluid," Proc. R. Soc. London, Ser. A **132**, 499-523 (1931).
[22] P. G. Drazin and W. H. Reid, *Hydrodynamic Stability* (Cambridge University Press, Cambridge, UK, 1981).
[23] M. P. Juniper, "The effect of confinement on the stability of two-dimensional shear flows," J. Fluid Mech. **565**, 171-195 (2006).
[24] M. P. Juniper, "The full impulse response of two-dimensional jet/wake flows and implications for confinement," J. Fluid Mech. **590**, 163-185 (2007).
[25] L. Biancofiore and F. Gallaire, "Influence of confinement on temporal stability of plane jets and wakes," Phys. Fluids **22**, 014106 (2010).